

Coexistence of magnetic order and valence fluctuations in the Kondo lattice system $\text{Ce}_2\text{Rh}_3\text{Sn}_5$.

M. B. Gamża^{1,2,3}, R. Gumeniuk^{2,4}, U. Burkhardt², W. Schnelle², H. Rosner², A. Leithe-Jasper², and A. Ślebarski^{3,5}

¹*Jeremiah Horrocks Institute for Mathematics, Physics and Astrophysics,*

University of Central Lancashire, Preston PR1 2HE, UK

²*Max-Planck Institute for Chemical Physics of Solids, D-01187 Dresden, Germany*

³*Institute of Physics, University of Silesia, 40-007 Katowice, Poland*

⁴*Institute of Experimental Physics, TU Bergakademie Freiberg, 09596 Freiberg, Germany and*

⁵*Centre for Advanced Materials and Smart Structures,
Polish Academy of Sciences, 50-950 Wrocław, Poland*

We report on the electronic band structure, structural, magnetic and thermal properties of $\text{Ce}_2\text{Rh}_3\text{Sn}_5$. Ce L_{III} -edge XAS spectra give direct evidence for an intermediate valence behaviour. Thermodynamic measurements reveal magnetic transitions at $T_{\text{N}1} \approx 2.9$ K and $T_{\text{N}2} \approx 2.4$ K. Electrical resistivity shows behaviour typical for Kondo lattices. The coexistence of magnetic order and valence fluctuations in a Kondo lattice system we attribute to a peculiar crystal structure in which Ce ions occupy two distinct lattice sites. Analysis of the structural features of $\text{Ce}_2\text{Rh}_3\text{Sn}_5$, together with results of electronic band structure calculations, thermodynamic and spectroscopic data indicate that at low temperatures only Ce ions from the Ce1 sublattice adopt a stable trivalent electronic configuration and show local magnetic moments that give rise to the magnetic ordering. By contrast, our study suggests that Ce2 ions exhibit a nonmagnetic Kondo-singlet ground state. Furthermore, the valence of Ce2 ions estimated from the Ce L_{III} -edge XAS spectra varies between +3.18 at 6 K and +3.08 at room temperature. Thus, our joined experimental and theoretical investigations classify $\text{Ce}_2\text{Rh}_3\text{Sn}_5$ as a multivalent charge-ordered system.

PACS numbers: 71.28.+d, 75.30.Mb, 71.27.+a, 79.60.-i, 71.20.Lp

Keywords: Kondo lattice, intermediate valence, mixed valence, electronic structure, magnetic, thermal and transport properties

I. INTRODUCTION

In Ce-based Kondo lattice systems a delicate interplay of localized and itinerant electronic degrees of freedom leads to a wealth of intriguing strongly correlated electron phenomena.^{1–6} Kondo lattice compounds contain Ce ions arranged periodically in a crystal lattice. Thus, local f -moments of the Ce^{3+} ions can mutually couple via the conduction electrons by means of the Ruderman-Kittel-Kasay-Yosida (RKKY) interaction.⁷ Simultaneously, the f -moments are screened by spins of conduction s -electrons. This antiferromagnetic (AFM) Kondo coupling drives the demagnetization of the f -electron states and leads to the formation of the Abrikosov-Suhl resonance near the Fermi level.^{1,2}

Both the RKKY interaction and Kondo effect depend on the coupling constant J_{s-f} of the local f -moments with the conduction electron states, with the characteristic temperatures $T_{\text{RKKY}} \sim J_{s-f}^2$ and $T_{\text{K}} \sim \exp(1/|J_{s-f}|)$, respectively.⁸ In the weak coupling limit, the magnetic interaction dominates over the Kondo spin-compensation and a magnetic ground state results.^{1–3} For medium J_{s-f} values, a strong competition between Kondo effect and magnetic interactions gives rise to diverse intriguing physical phenomena, including magnetism with reduced moments,³ non-Fermi liquid behaviour⁵ or magnetically driven superconductivity.^{3,4} In turn, in the strong coupling limit, the Kondo effect predominates and leads to a nonmagnetic heavy-fermion

(HF) ground state.¹ Importantly, for large J_{s-f} values the strong hybridization between the $4f$ and other conduction band states together with a proximity of the $4f$ level to the Fermi energy may also trigger instabilities of the charge configuration of the Ce ions, resulting in an intermediate valence (IV) behaviour.⁶ Thus, physical properties of IV systems are governed by both spin fluctuations due to Kondo effect and charge fluctuations between $4f^0$ and $4f^1$ configurations that are nearly degenerate in energy.

While vast majority of Ce-based intermetallic compounds contains either trivalent or intermediate-valent Ce ions, only for a limited number of systems a coexistence of both species has been reported. Examples of such materials include Ce_2RuZn_4 ^{9,10}, $\text{Ce}_3\text{Ni}_2\text{Ge}_7$ ¹¹, $\text{Ce}_{23}\text{Ru}_7\text{X}_4$ ($X = \text{Mg}, \text{Cd}$)^{12,13}, CeRuSn ^{14–16}, Ce_5Sn_3 ¹⁷, Ce_7T_3 (T -transition metal)¹⁸, $\text{Ce}_{4-x}\text{Ru}_4\text{Ge}_{12+x}$ ¹⁹. These systems often exhibit remarkable electronic and magnetic properties related to a mixture of Ce ions with long and extraordinarily short distances to the neighbouring atoms due to a peculiar bonding situation. Bearing this distinctive structural feature in mind, we started systematic investigations aiming at finding novel intermetallic compounds with highly unconventional magnetic behaviour resulting from the presence of Ce ions in different valence states.

We focused our search on the system Ce-Rh-Sn as it is rich in ternary phases that show a full spectrum of strongly correlated electron phenomena related to various strength of hybridization between

Ce $4f$ and other valence band states.^{20–27} CeRhSn₂, Ce₅Rh₄Sn₁₀, CeRh₂Sn₄ and Ce₃Rh₄Sn₁₃ are magnetically ordered Kondo lattice systems.^{20–23} In contrast, for Ce_{3+x}Rh₄Sn_{13-x} ($0.2 \lesssim x \lesssim 0.6$) no sign of Kondo effect or long range magnetic order was found even down to 0.4 K.²⁵ In turn, in CeRhSn the Ce ions are in an IV state.^{26,27}

Here, we report on Ce₂Rh₃Sn₅ that crystallizes in the orthorhombic Y₂Rh₃Sn₅ type of structure, where Y ions occupy two distinct crystallographic sites.^{28,29} An early study revealed a moderate HF behaviour ($\gamma \approx 150$ mJ Ce-mol⁻¹K⁻²) with a magnetic transition at $T_N \approx 5$ K (from resistivity), 4 K (from magnetic susceptibility) or 2.5 K (from heat capacity).²⁸ Our single crystal X-ray diffraction (XRD) study unveils extraordinarily short Ce–Rh contacts indicative of valence larger than 3+ for one Ce site. Interestingly, the local environment of Ce atoms from the second sublattice is very similar to that in CeRh₂Sn₄, a magnetic Kondo lattice system with trivalent Ce ions and $T_N \approx 3.2$ K.²³ Motivated by these results, we performed a combined experimental and theoretical study on Ce₂Rh₃Sn₅ based on thermodynamic measurements and spectroscopic data together with first principles electronic structure calculations aiming at exploring its complex structural and magnetic properties.

II. METHODS

A. Experimental

Polycrystalline samples of Ce₂Rh₃Sn₅ with total weight of about 2 g were prepared from ingots of cerium (Ames, 99.9 wt.%), rhodium granules (ChemPur, 99.9 wt.%) and tin foil (ChemPur, 99.995 wt.%). Stoichiometric amounts of the elemental metals were arc-melted on a water cooled copper hearth in an ultra-high purity Ar atmosphere with a Zr getter (heated above the melting point). The sample was remelted several times to promote homogeneity and heat-treated at 800°C for 14 days in a sealed Ta tube enclosed in an evacuated quartz tube. Almost no mass loss (below 0.02%) occurred during the melting and annealing processes.

All manipulations related to preparation of the sample and its storage were performed in a argon-filled glove box (MBRAUN, p(O₂/H₂O) ≤ 1 ppm) in order to prevent the oxidation.

The quality of the sample was examined by means of powder XRD measurements and metallographic investigations. Details of these studies are included in the Supplementary Information³⁰. Powder XRD pattern indicates that the sample is nearly single phased. Microprobe measurements revealed the chemical composition that corresponds to Ce_{2.01(1)}Rh_{3.00(2)}Sn_{5.00(2)} and thus confirms the desired stoichiometry.

An irregularly shaped crystal was mechanically extracted from the annealed ingot. Single crystal XRD

study was performed at room temperature using an Xcalibur E Single Crystal Diffractometer. Details concerning data collection and handling are summarized in Table I. Structure refinements were carried out using the Jana2006 program.³³

The Ce L_{III} XAS spectra were recorded in transmission arrangement at the EXAFS beamline C of HASYLAB at DESY at the temperatures of 80 K and 293 K. The wavelength selection was realized using the four-crystal mode which yielded an experimental resolution of ~ 2 eV (FWHM) at the Ce L_{III} threshold of 5723 eV. Powdered samples of Ce₂Rh₃Sn₅ were mixed with small amounts of B₄C and mounted on 1 cm² window sample holders using paraffin wax. Two series of measurements performed using different sample powders at ambient temperature and at low temperatures down to 6 K using a helium gas flow cryostat gave consistent results. Experimental data were recorded with CePO₄ as the external reference compound with Ce³⁺ ions. The Ce L_{III} XAS spectra were evaluated using the Athena program package³⁴.

XPS experiments were performed at room temperature using a PHI 5700 ESCA spectrometer with monochromatized Al K α radiation. The energy resolution was about 0.4 eV. The polycrystalline sample was broken under a high vacuum of 6×10^{-10} Torr immediately before measuring the spectra. Binding energies were referenced to the Fermi level ($E_F = 0$). Calibration of the spectra was performed according to Ref. 35.

The magnetization studies were carried out in a SQUID magnetometer (MPMS XL-7, Quantum Design) at temperatures between 1.8 K and 400 K in magnetic fields up to 70 kOe. Electrical resistivity measurements were performed with a standard dc four-probe setup. Heat capacity was determined by a relaxation-type method using a commercial system (PPMS, Quantum Design).

B. Computational

The electronic structure of Ce₂Rh₃Sn₅ was studied using the Full Potential Local Orbital (FPLO) Minimum Basis code³⁶. Scalar-relativistic calculations based on Density Functional Theory (DFT) were performed within the local (spin) density approximation [L(S)DA] using the Perdew and Wang³⁷ parametrization of the exchange-correlation (XC) potential. The strong Coulomb correlation within the Ce $4f$ shell was also treated in a mean field approximation using the LSDA+ U method³⁸ with the around mean field double counting scheme. The Coulomb repulsion U and exchange constant J for the $4f$ states of both types of Ce atoms were assumed to be 1–8 eV and 1 eV, respectively. Thus, the effective $U_{\text{eff}}=U-J$ was from the range of 0–7 eV. The Brillouin zone sampling was based on 198 \mathbf{k} -points in the irreducible wedge (2000 points in the full zone). A series of calculations with an increasing density

TABLE I. Crystallographic data for $\text{Ce}_2\text{Rh}_3\text{Sn}_5$.

Empirical formula	$\text{Ce}_2\text{Rh}_3\text{Sn}_5$
Structure type	$\text{Y}_2\text{Rh}_3\text{Sn}_5$
Space group	$Cmc2_1$ (No. 36)
Lattice parameters ^a	$a = 4.4992(1) \text{ \AA}$ $b = 26.4839(7) \text{ \AA}$ $c = 7.2160(2) \text{ \AA}$
Unit cell volume, ^a V	$859.83(4) \text{ \AA}^3$
Formula units/cell, Z	4
Crystal density, ρ	9.151 g cm^{-3}
Temperature	$295(5) \text{ K}$
Diffraction system	Xcalibur E, four-circle Kappa Sapphire CCD Detector (Xcalibur)
Radiation, λ	$\text{Mo } K\alpha$, 0.71073 \AA
Range in h, k, l	$\pm 9, \pm 52, \pm 14$
$R(eq\upsilon)/R(\sigma)$	$0.078/0.018$
$2\theta_{min}/2\theta_{max}$	$4.17/45.49$
Observation criteria	$F(hkl) > 3.00\sigma(F)$
Resolution d (\AA)	0.45
Absorption correction	face-based, analytical ³¹
Absorption coefficient	30.194
$N(hkl)$ measured	71975
$N(hkl)$ unique	3939
Extinction method	isotropic type 2 correction ³²
Extinction coefficient	4070(70)
Number of parameters	63
Goodness-of-fit (GOF)	1.94
R	2.25%
wR	3.28%

^apowder data

of the \mathbf{k} -mesh was performed to ensure the convergence of the total energy with respect to the \mathbf{k} -grid.

Based on the band structure results we estimated the theoretical XPS valence band spectra. The partial l -resolved densities of states obtained using the LDA and the LSDA+U ($U=6 \text{ eV}$, $J=1 \text{ eV}$) methods were weighted by their respective photoionisation cross-sections³⁹. The results were multiplied by the Fermi-Dirac function for 300 K and convoluted by Lorentzians with a full width at half maximum (FWHM) of 0.4 eV to account for the instrumental resolution, thermal broadening and the lifetime effect of the hole states.

III. RESULTS AND DISCUSSION

A. Crystal structure

Refinement of the single crystal XRD data shows that $\text{Ce}_2\text{Rh}_3\text{Sn}_5$ crystallizes with the non-centrosymmetric orthorhombic $\text{Y}_2\text{Rh}_3\text{Sn}_5$ type of structure (space group $Cmc2_1$), in agreement with earlier reports.^{28,29} The crys-

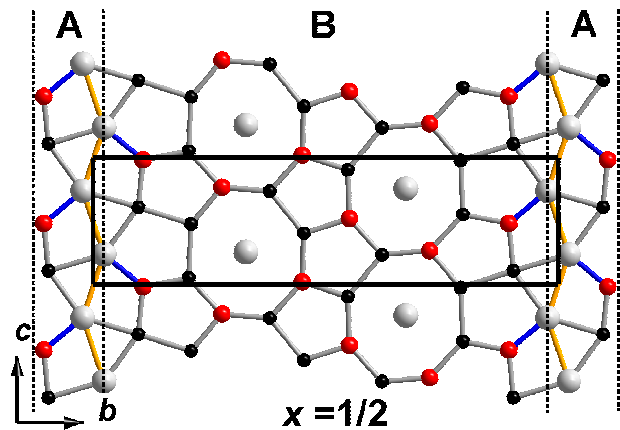


FIG. 1. (Color online) The planar layer in the structure of $\text{Ce}_2\text{Rh}_3\text{Sn}_5$ occurring at $x = 1/2$. Fragment A: a chain of interconnected Ce atoms (yellow line) and edge sharing tetragons and triangles; fragment B: condensed empty pentagons and octagons of Rh (red) and Sn (black) centred by Ce (grey) atoms.

tallographic details of the refinement are given in Table I, atomic coordinates and anisotropic displacement parameters – in Table II and interatomic distances in Table III.

The $\text{Y}_2\text{Rh}_3\text{Sn}_5$ type is a layered structure consisting of two analogical layers shifted by $1/2$ of the translation in the bc -plane and alternating along x -direction. As indicated in Fig. 1, each layer consists of two main fragments: A (a chain of interconnected Y_2/Ce_2 atoms and edge sharing tetragons and triangles) and B (condensed pentagons and octagons). The octagons are centred by heavy Y_1/Ce_1 atoms, while pentagons remains empty. The B-fragments are very similar to layers formed by octagons and pentagons in the structure of the NdRh_2Sn_4 type. The close structural relationship of $\text{Y}_2\text{Rh}_3\text{Sn}_5$ and NdRh_2Sn_4 types is widely discussed in the literature.^{23,29,40}

The interatomic distances in the structure of $\text{Ce}_2\text{Rh}_3\text{Sn}_5$ (Table III) mostly correlate well with the sum of atomic radii of the elements [$r_{(\text{Ce})} = 1.825 \text{ \AA}$; $r_{(\text{Rh})} = 1.34 \text{ \AA}$; $r_{(\text{Sn})} = 1.41 \text{ \AA}$]⁴¹. The Sn-Sn contacts are slightly longer than 2.81 \AA , while the Rh-Sn distances are shortened by about 4-5%, which assumes the formation of covalently bonded Rh-Sn framework in the investigated structure. The shrinking of Ce-Sn contacts is of 1-2%, assuming also a weak interaction.

The most intriguing feature of the $\text{Ce}_2\text{Rh}_3\text{Sn}_5$ structure is the shortened Ce2-Rh2 distance by nearly 11% as compared to the sum of atomic radii of Ce and Rh. Such extraordinarily short Ce2-Rh contacts indicate that the valence of Ce2 ions should be larger than $+3$.^{6,27,42,43} In turn, for Ce1 ions all the Ce1-Sn and Ce1-Rh distances are nearly equal to the sum of corresponding atomic radii. This suggests that the electronic configuration for Ce1 ions is close to $4f^1$, i.e. Ce^{+3} . Thus, the analysis of the crystal structure indicates that $\text{Ce}_2\text{Rh}_3\text{Sn}_5$ may

TABLE II. Atomic positional and displacement parameters for $\text{Ce}_2\text{Rh}_3\text{Sn}_5$ (Note: $B_{12}=B_{23}=0.$) All atoms are located at $4a$ (0,y,z) Wyckoff positions. The experimental structural data are compared to those derived from the band structure calculations in the LDA approximation. The free parameters in atomic coordinates obtained from the computational study were rounded to three significant digits.

Atom	experiment							LDA	
	y	z	B_{11}	B_{22}	B_{33}	B_{23}	B_{iso}	y	z
Ce1	0.32754(1)	0.27397(5)	0.72(1)	0.77(1)	0.98(1)	-0.02(1)	0.82(1)	0.330	0.274
Ce2	0.02426(1)	0.25076(4)	0.93(1)	0.77(1)	0.81(1)	-0.08(1)	0.84(1)	0.026	0.239
Rh1	0.72296(2)	0.28274(6)	0.75(1)	0.74(1)	0.87(2)	-0.06(1)	0.79(1)	0.723	0.280
Rh2	0.10594(2)	0.00000(6)	1.06(2)	0.82(1)	0.94(2)	0.01(1)	0.94(1)	0.103	0.999
Rh3	0.44897(2)	0.03180(6)	0.78(1)	0.82(1)	0.80(2)	0.00(1)	0.80(1)	0.450	0.015
Sn1	0.21037(1)	0.49104(5)	0.80(1)	0.82(1)	0.73(1)	-0.07(1)	0.78(1)	0.210	0.491
Sn2	0.20563(1)	0.07177(6)	0.71(1)	0.82(1)	0.79(1)	0.09(1)	0.77(1)	0.205	0.065
Sn3	0.62182(1)	0.25218(6)	1.41(1)	0.69(1)	0.93(1)	-0.09(1)	1.01(1)	0.622	0.242
Sn4	0.45116(1)	0.41543(6)	0.86(1)	0.73(1)	0.77(1)	0.01(1)	0.79(1)	0.452	0.400
Sn5	0.09635(1)	0.62444(6)	0.77(1)	0.76(1)	0.99(1)	0.16(1)	0.84(1)	0.096	0.618

TABLE III. Selected interatomic distances in $\text{Ce}_2\text{Rh}_3\text{Sn}_5$.

Atoms	d (Å)	Atoms	d (Å)
Ce1 - 2Sn1	3.1979(4)	1Ce1	3.4733(5)
		1Sn2	3.0255(5)
2Sn5	3.2060(4)	1Sn5	3.1670(5)
2Sn2	3.2310(4)	2Sn2	3.2155(4)
1Sn4	3.4268(5)	2Rh1	2.7250(3)
1Sn1	3.4733(5)	1Rh1	2.7452(6)
1Sn2	3.5402(5)	Sn2 - 2Ce1	3.2310(4)
2Rh2	3.2885(4)	1Ce1	3.5402(5)
Ce2 - 2Sn4	3.1954(3)	1Sn1	3.0255(5)
1Sn5	3.3012(5)	2Sn1	3.2155(4)
1Sn5	3.3190(5)	1Rh2	2.6885(6)
2Sn4	3.3656(4)	2Rh1	2.7537(4)
2Sn3	3.4243(4)	1Rh1	2.8132(6)
1Rh2	2.8180(5)	Sn3 - 2Ce2	3.4243(4)
2Rh3	3.1091(4)	1Sn4	3.1024(5)
Rh1 - 1Sn3	2.6854(5)	1Rh1	2.6854(5)
2Sn1	2.7250(3)	1Rh3	2.7522(6)
1Sn1	2.7452(6)	2Rh2	2.9226(4)
2Sn2	2.7537(4)	Sn4 - 2Ce2	3.1954(3)
1Sn2	2.8132(6)	2Ce2	3.3656(4)
Rh2 - 1Ce2	2.8180(5)	1Ce1	3.4268(5)
2Ce1	3.2885(4)	1Sn3	3.1024(5)
1Sn2	2.6885(6)	1Rh3	2.7665(6)
1Sn5	2.7196(6)	1Rh3	2.7729(6)
2Sn4	2.7774(3)	2Rh2	2.7774(3)
2Sn3	2.9226(4)	Rh3 - 2Ce2	3.1091(4)
Rh3 - 2Ce2	3.1091(4)	Sn5 - 2Ce1	3.2060(4)
2Sn5	2.6350(3)	1Ce2	3.3012(5)
1Sn3	2.7522(6)	1Ce2	3.3190(5)
1Sn4	2.7665(6)	1Sn1	3.1670(5)
1Sn4	2.7729(6)	2Rh3	2.6350(3)
Sn1 - 2Ce1	3.1979(4)	1Rh2	2.7196(6)

be a mixed valence, IV or even a multivalent charge-ordered system. The last scenario assumes a static ordering of trivalent and intermediate-valent Ce ions in two distinct lattice sites and was proposed for systems such as Ce_2RuZn_4 ^{9,10}, $\text{Ce}_3\text{Ni}_2\text{Ge}_7$ ¹¹, $\text{Ce}_{23}\text{Ru}_7\text{X}_4$ ($X = \text{Mg}, \text{Cd}$)^{12,13}, Ce_5Sn_3 ¹⁷, YbPtGe_2 .⁴⁴

To inspect the valence states of Ce ions in $\text{Ce}_2\text{Rh}_3\text{Sn}_5$ more closely, we performed spectroscopic measurements.

B. Ce L_{III} XAS

Fig. 2 presents the near-edge regime of Ce L_{III} XAS spectra for $\text{Ce}_2\text{Rh}_3\text{Sn}_5$ that were recorded at several temperatures between 6 K and 300 K. Although the spectra are dominated by 'white line' at the energy of ~ 5726 eV corresponding to $4f^1$ configuration of Ce^{3+} , there is also an additional contribution at the energy of nearly +9 eV above the 'white line' maximum that indicates the presence of Ce^{4+} species with electron configuration $4f^0$. Increasing temperature from 6 K to 300 K leads to a gradual reduction of the high energy contribution due to $4f^0$ configuration of Ce^{4+} and a simultaneous slight increase in intensity of the 'white line', as shown in Fig. 2b. Such a progressive shift of the spectral weight to lower energies implies an IV behaviour. Although the temperature induced changes in the Ce L_{III} XAS spectra are rather small, similar slight effects were reported for many Ce-based IV compounds.^{6,43,45,46}

Deconvolution of the Ce L_{III} XAS spectra (example in Fig. 2a) indicates that the mean Ce valence in $\text{Ce}_2\text{Rh}_3\text{Sn}_5$ decreases from +3.09(1) at 6 K to +3.04(1) at ambient temperature, with the most rapid changes taking place at temperatures of 100 K (see lower inset in Fig. 2b). However, since the measured spectra contain signal originating from all Ce ions, the obtained values of Ce valence in $\text{Ce}_2\text{Rh}_3\text{Sn}_5$ should be interpreted as the *average* valence for Ce ions from two distinct lattice sites. There-

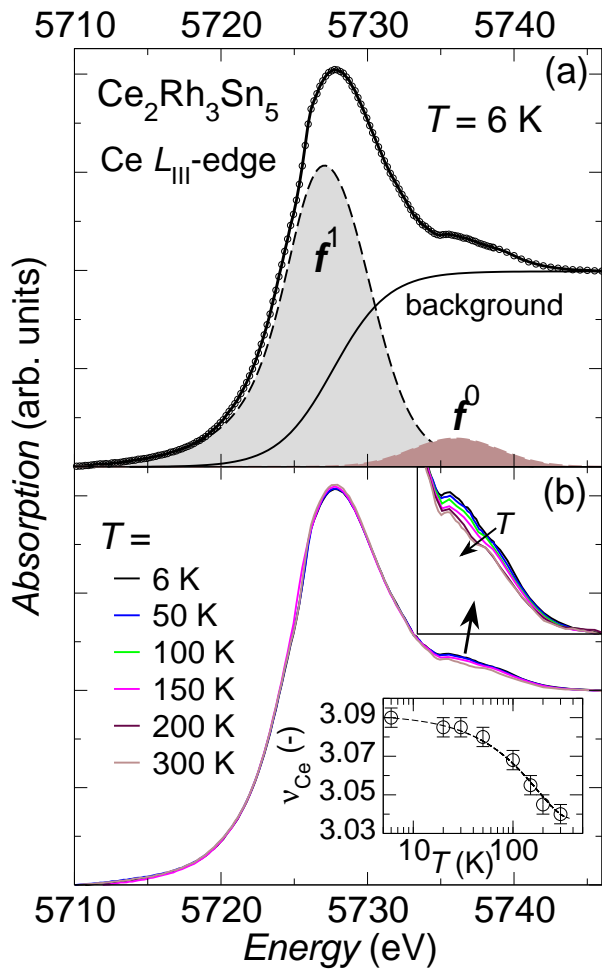


FIG. 2. (Color online) Near-edge regime of Ce L_{III} XAS spectra for $\text{Ce}_2\text{Rh}_3\text{Sn}_5$. Panel a shows deconvolution of the normalized spectrum recorded at $T = 6$ K. The contributions due to f^1 and f^0 configurations are indicated by beige or grey fields underneath the dashed lines, while the solid black line represents the arctan function that accounts for transitions of $2p_{3/2}$ electrons to the extended conduction states. Panel b depicts normalized Ce L_{III} XAS spectra measured at various temperatures between 6 K and 300 K. The changes in intensity of the f^0 contribution are enlarged in the upper inset, with the arrow indicating the direction of increasing temperature. Lower inset of panel b displays calculated changes of Ce valence as a function of temperature. The dashed line was guided to the eye.

fore, assuming that Ce1 ions are trivalent in the entire temperature range, the valence of Ce2 species should vary between +3.18 at 6 K and +3.08 at ~ 300 K. We note that similar Ce valence was reported for nonmagnetic IV compounds such as CeRhSi_2 ⁴³, $\text{Ce}_2\text{Ni}_3\text{Si}_5$ ⁴⁷, $\text{CeMo}_2\text{Si}_2\text{C}$ ⁴⁸.

To shed more light on the character of Ce $4f$ states in $\text{Ce}_2\text{Rh}_3\text{Sn}_5$, we performed X-ray photoelectron spectroscopy measurements.

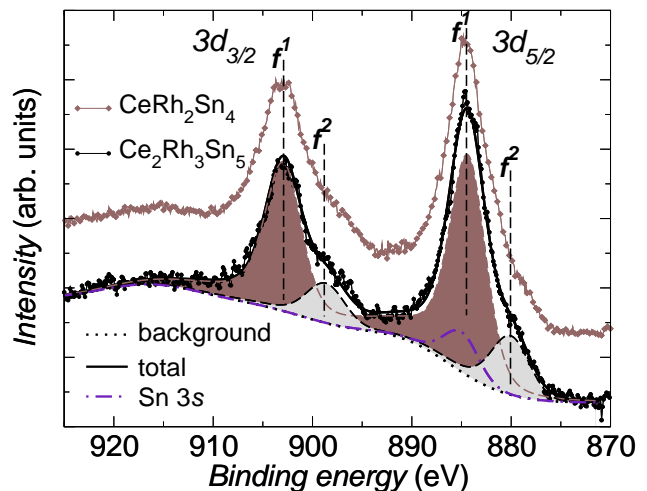


FIG. 3. (Color online) The Ce $3d$ XPS spectra for $\text{Ce}_2\text{Rh}_3\text{Sn}_5$ and CeRh_2Sn_4 . The spin-orbit components $3d_{3/2}$ and $3d_{5/2}$ as well as the f^1 and f^2 contributions are labelled. The deconvolution of the spectrum for $\text{Ce}_2\text{Rh}_3\text{Sn}_5$ is shown.

C. Ce $3d$ XPS

Fig. 3 shows room temperature Ce $3d$ XPS spectrum for $\text{Ce}_2\text{Rh}_3\text{Sn}_5$ together with the data for the structurally related compound CeRh_2Sn_4 . Due to the spin-orbit (SO) coupling, Ce $3d$ states give rise to two sets of photoemission lines that correspond to the $j = 3/2$ and $j = 5/2$ components of final states. Each of these SO sets consists of two distinct contributions labelled as f^1 and f^2 . The f^1 components originate from the screening of the core hole by conduction electrons. The f^2 satellites arise when an electron is transferred from extended valence band states to the $4f$ states during photoemission process in order to screen the hole in the core shell. Since the probability of such processes depends on the coupling of the $4f$ levels to the other states near the Fermi level,⁴² the presence of the pronounced f^2 peaks indicates that there is a notable hybridization between the Ce $4f$ and conduction band states in $\text{Ce}_2\text{Rh}_3\text{Sn}_5$.

There are no additional peaks in the Ce $3d$ XPS spectrum of $\text{Ce}_2\text{Rh}_3\text{Sn}_5$ in a distance of ~ 11 eV from the main photoemission lines, that could be assigned to the $4f^0$ final states. This result may seem to contradict the mean Ce valence of +3.04 at ambient temperature obtained from our XAS measurements (see Section III B). We note, however, XPS measurements with energy resolution of 0.4 eV may not show weak f^0 contributions. Our simulations (not shown) indicate that only peaks with intensities greater than $\sim 5\%$ of the combined intensity of f^1 and f^2 contributions should be detectable in the Ce $3d$ XPS spectrum of $\text{Ce}_2\text{Rh}_3\text{Sn}_5$, whereas weaker f^0 contributions should be hidden in the background signal and experimental noise. Thus, the absence of f^0 -type peaks implies the mean occupancy of the Ce $4f$ shell $n_f \gtrsim 0.95$ at room temperature, which agrees with the

results of our XAS study (see Section III B).

Deconvolution of the Ce $3d$ XPS spectrum was performed on the basis of Doniach-Sunjić theory⁴⁹. The intensity ratio $I(3d_{5/2})/I(3d_{3/2}) = 3/2$ was fixed during the fitting, as required by the quantum-mechanical rules. The SO split $\delta_{S-O} \approx 18.6$ eV was assumed. A Tougaard-type background⁵⁰ was subtracted from the XPS data. A small peak due to the Sn $3s$ states located at the binding energy of 885 eV was included in the fit, with the intensity determined by the stoichiometry of the compound $\text{Ce}_2\text{Rh}_3\text{Sn}_5$. Model calculations of Gunnarsson and Schönhammer (GS)^{42,51} were used to calculate the value of the Δ parameter describing the hybridization strength between the Ce $4f$ shell and conduction electron states from relative intensities of the f^2 peaks. Such a procedure yielded $\Delta \approx 100$ meV, which should be considered as the *average* hybridization parameter for Ce ions occupying two lattice sites in $\text{Ce}_2\text{Rh}_3\text{Sn}_5$.

The obtained Δ value is comparable to those found in systems with Ce in an IV state ($\Delta \gtrsim 100$ meV)^{26,27,42} and is notably stronger than in other compounds from the ternary Ce-Rh-Sn system with trivalent Ce ions ($\Delta \lesssim 80$ meV)^{20,22-25}. In particular, the Δ value for $\text{Ce}_2\text{Rh}_3\text{Sn}_5$ is larger than that for the structurally related compound CeRh_2Sn_4 with Ce^{3+} , as evidenced directly by larger intensities of f^2 satellites in the Ce $3d$ XPS spectra (see Fig. 3).

Despite the strong hybridization Δ and valence fluctuations revealed by our spectroscopic investigations, thermodynamic measurements indicate a magnetic ground state for $\text{Ce}_2\text{Rh}_3\text{Sn}_5$.

D. Magnetic measurements

Figures 4 and 5 present results of a *dc* magnetization study on polycrystals of $\text{Ce}_2\text{Rh}_3\text{Sn}_5$. The $M(T)$ measured in weak magnetic fields increases rapidly at temperatures below ~ 2.9 K, suggestive of an onset of magnetic order (see Fig. 4a). Closer inspection shows that the $M(T)$ grows even faster at $T \leq 2.4$ K. This points to a change in magnetic structure at 2.4 K, in agreement with our specific heat data that revealed two anomalies at $T_{N1} \approx 2.9$ K and $T_{N2} \approx 2.4$ K (see Section III E). The presence of two magnetic transitions in $\text{Ce}_2\text{Rh}_3\text{Sn}_5$ provides an explanation for the discrepancy between ordering temperatures reported by Patil *et al.*²⁸ based on the specific heat and magnetization data.

Isothermal magnetization curves measured at temperatures below 3 K show distinct hysteresis between the data collected with increasing and decreasing field strengths. The illustrative $M(H)$ data recorded at $T = 1.8$ K are shown in Fig. 4b. Both the remanence magnetization M_r and the coercive field decrease gradually with increasing temperature and finally diminish at $T_{N1} \approx 2.9$ K (see the lower inset of Fig. 4b). However, the magnetization in the ordered states is very small, about two orders of magnitude smaller than magnetization values expected

for a ferromagnetic order that involves one magnetic ion per formula unit with $S = 1/2$. Thus, the magnetization measurements suggest an AFM ordering with only small canting in $\text{Ce}_2\text{Rh}_3\text{Sn}_5$ at temperatures below 2.4 K, with the canting becoming even smaller between 2.4 K and 2.9 K.

At high temperatures the magnetic susceptibility $\chi = M/H$ does not depend on the applied magnetic field and resembles behaviour expected for a local moment paramagnet (see the inset of Fig. 4). As shown in the inset of Fig. 5, at temperatures between ~ 170 K and 400 K the $\chi^{-1}(T)$ follows a modified Curie-Weiss law:

$$\chi(T) = \frac{C_{\text{HT}}}{T - \theta_{\text{HT}}} + \chi_{0-\text{HT}}, \quad (1)$$

with $\chi_{0-\text{HT}} \approx 8 \times 10^{-5}$ emu/mol, the paramagnetic Weiss temperature $\theta_{\text{HT}} \approx -103$ K and the Curie constant $C_{\text{HT}} = 1.60$ emu K/mol. The obtained C_{HT} value corresponds to the fluctuating magnetic moment of $2.51 \mu_B$ per Ce, which is very close to the effective moment of $2.53 \mu_B/\text{Ce}$ expected for free Ce^{3+} ions. Thus, the magnetic measurements indicate that at temperatures above ~ 170 K the valence of Ce ions in $\text{Ce}_2\text{Rh}_3\text{Sn}_5$ is close to $3+$ and all the Ce ions bear localized magnetic moments.

The small positive $\chi_{0-\text{HT}}$ is in-line with metallic properties of $\text{Ce}_2\text{Rh}_3\text{Sn}_5$. The $\chi_{0-\text{HT}}$ is the sum of the diamagnetic susceptibility of the closed-shells and the conduction electron contributions. Assuming that for tin $\chi_{\text{dia}}(\text{Sn}^{4+}) = -16 \times 10^{-6}$ emu/mol, for cerium $\chi_{\text{dia}}(\text{Ce}^{3+}) = -20 \times 10^{-6}$ emu/mol and for rhodium $\chi_{\text{dia}}(\text{Rh}^{4+}) = -18 \times 10^{-6}$ emu/mol,⁵² the sum of the diamagnetic core increments yields -174×10^{-6} emu/mol. Thus, the rough estimate of the electronic Pauli susceptibility χ_P , after correcting for the Landau electron diamagnetism $\chi_L = -\frac{1}{3} \chi_P$ and the core-level diamagnetism, gives 381×10^{-6} emu/mol. This value corresponds to the $\text{DOS}(E_F) \approx 11.8$ states eV^{-1} f.u.⁻¹ which is comparable to the value of the $\text{DOS}(E_F)$ obtained from our electronic band structure calculations (Fig. 9).

At lower temperatures, the experimental $\chi(T)$ data can be well described by the modified Curie-Weiss law (see Fig. 5) with a small negative Weiss temperature $\theta_{\text{LT}} \approx -6$ K of the order of T_{N1} , $\chi_{\text{LT}} \approx 0.0039$ emu/mol and the Curie constant $C_{\text{LT}} = 0.48$ emu K/mol, which is strongly reduced as compared to the value of 1.60 emu K/mol expected for full moments of Ce^{3+} ions. The hefty lowering of the effective fluctuating moment accompanied by a strong enhancement of the Pauli susceptibility upon lowering temperature points to the delocalization of $4f$ electrons from some of Ce ions in $\text{Ce}_2\text{Rh}_3\text{Sn}_5$. The large negative Weiss temperature $\theta_{\text{HT}} \approx -110$ K indicates that there is a strong AFM coupling of the local $4f$ moments with conduction band states. In Ce-based Kondo lattice systems, this interaction drives the demagnetization of the f -electron states and can lead to the formation of a nonmagnetic Kondo-singlet state, for which an enhanced Pauli-like magnetic

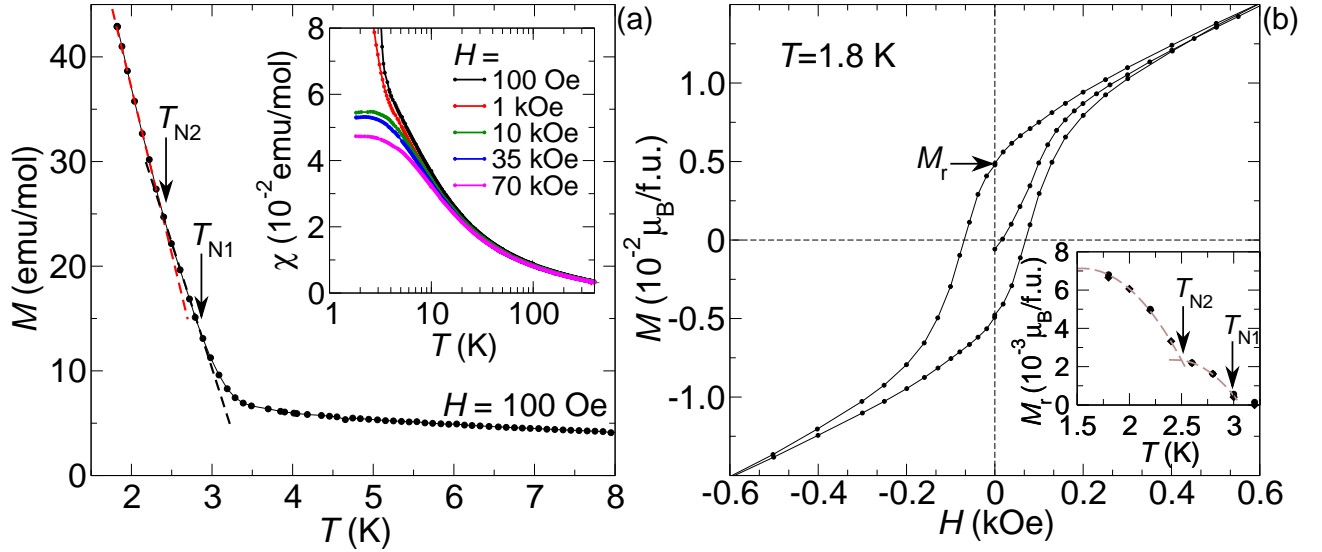


FIG. 4. (Color online) Results of *dc* magnetization measurements for $\text{Ce}_2\text{Rh}_3\text{Sn}_5$. Panel a shows the low temperature part of the $M(T)$ measured in magnetic field of 100 Oe. Two distinct changes in slope of the $M(T)$ curve suggestive of magnetic transitions are indicated. The inset displays the magnetic susceptibility measured in a number of magnetic fields between 100 Oe and 70 kOe and plotted as a function of temperature on a logarithmic scale. Panel b depicts the full magnetization loop at $T = 1.8$ K. Inset shows values of the remanence magnetization at various temperatures. The dashed lines are guided to the eye.

susceptibility results from the presence of a narrow peak in the quasiparticle DOS near the Fermi energy due to the Abrikosov–Suhl resonance.^{6,53}

Since there are two distinct Ce sites in $\text{Ce}_2\text{Rh}_3\text{Sn}_5$ (see Section III A), we attempted to fit the experimental magnetic susceptibility in a broad temperature range as:

$$\chi(T) = \frac{C}{T - \theta} + \chi_{\text{Ce2}}(T), \quad (2)$$

with the first term describing Curie–Weiss behaviour anticipated for local moments of Ce^{3+} ions from Ce1 sublattice and the second term $\chi_{\text{Ce2}}(T)$ included to account for magnetic susceptibility of Ce2 ions calculated based on $\chi(T/T_0)/\chi(0)$ curve obtained by Rajan⁵⁴ for trivalent Ce impurities ($j = 5/2$) embedded in a sea of conduction electrons. Here, T_0 stands for a characteristic temperature that reflects the strength of coupling between the Ce 4*f* and conduction band states, and $\chi(0)$ denotes the Pauli-like magnetic susceptibility of a non-magnetic Kondo-singlet state at zero temperature. A very good fit to the experimental $\chi(T)$ data at temperatures between ~ 10 K and 400 K was achieved assuming $T_0 \approx 280$ K, $\chi(0) \approx 0.003$ emu/mol, the paramagnetic Weiss temperature $\theta \approx -6$ K and the Curie constant $C = 0.48$ emu K/mol-Ce (see Fig. 4).

The negative Weiss temperature of -6 K is comparable to the magnetic ordering temperature and concurs with the dominance of weak AFM exchange interactions between local magnetic moments of Ce ions from the Ce1 sublattice. The estimated C value corresponds to the fluctuating moment of $1.96 \mu_B$ per Ce1, which is somewhat smaller than the magnetic moment of $2.54 \mu_B$ ex-

pected for free Ce^{3+} ions. We note that the local environment of Ce1 ions in the crystal lattice of $\text{Ce}_2\text{Rh}_3\text{Sn}_5$ is very similar to that in CeRh_2Sn_4 ,²³ an antiferromagnet with well localized Ce^{3+} moments. Since for CeRh_2Sn_4 the effective fluctuating moment decreases at temperatures below ~ 150 K due to a thermal depopulation of excited crystal field levels from the $j = 5/2$ multiplet of Ce^{3+} ions,²³ we suspect that the effective moment derived from the fit of the $\chi(T)$ for $\text{Ce}_2\text{Rh}_3\text{Sn}_5$ using Eq. 2 may be influenced by crystal electric field (CEF) effect on the magnetic Ce1 ions.

Since Eq. 2 does not consider CEF effects, the reliability of the performed fit is rather limited, especially regarding the detailed temperature dependence of the χ_{Ce2} term which is small as compared to the magnetic susceptibility originating from local magnetic moments of Ce1 ions in $\text{Ce}_2\text{Rh}_3\text{Sn}_5$. In addition, Eq. 2 does not account for the influence of valence fluctuations revealed by the XAS measurements (see Section III B) on the magnetic susceptibility due to Ce2 ions in $\text{Ce}_2\text{Rh}_3\text{Sn}_5$. Nevertheless, the temperature of the maximum in the $\chi_{\text{Ce2}}(T)$ derived from the fit of ~ 80 K is close to the value of the ratio $C(\text{Ce}^{3+})/(3\chi(0)) \approx 89$ K, ($C(\text{Ce}^{3+})$ is the Curie constant for Ce^{3+}), as expected for IV systems with nearly trivalent Ce.⁶ Furthermore, the maximum in the $\chi_{\text{Ce2}}(T)$ occurs in the same temperature range in which our XAS study revealed the fastest changes in Ce valence in $\text{Ce}_2\text{Rh}_3\text{Sn}_5$. This finding agrees with the observation of Lawrence *et al.*,⁶ that a single energy scale describes both charge and spin excitations associated with intermediate-valent Ce ions in systems with Ce valence close to 3+. Finally, it is worthwhile to note that

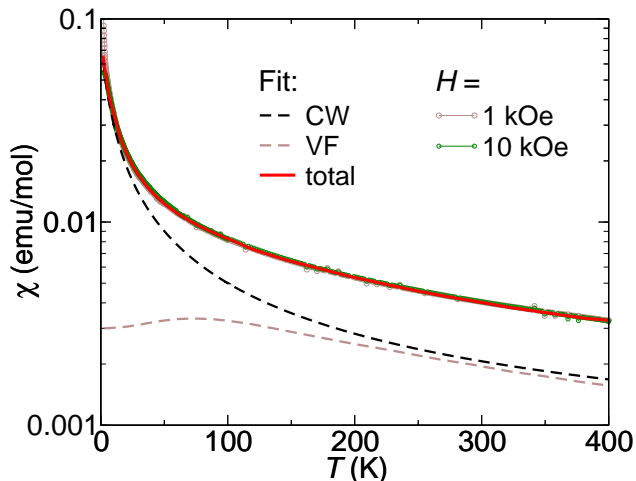


FIG. 5. (Color online) The *dc* magnetic susceptibility of $\text{Ce}_2\text{Rh}_3\text{Sn}_5$ measured in magnetic fields of 1 kOe (brown circles) and 10 kOe (green circles), together with the fit using Eq. 2 (thick solid red line). The Curie–Weiss–type contribution χ_{CW} due to Ce1 sublattice and the χ_{Ce2} term estimated based on calculations of Rajan⁵⁴ to account for the magnetic susceptibility originating from Ce2 ions are indicated with black and brown dashed lines, respectively. The solid blue line represents the best fit to the $\chi(T)$ data at temperatures of 8–85 K by using the modified Curie–Weiss law. The inset shows $\chi^{-1}(T)$ in a magnetic field of 10 kOe (green circles) together with the fit by using the modified Curie–Weiss law that covers the data above ~ 170 K (dashed red line).

the $\chi_{\text{Ce2}}(T)$ term obtained from the fit closely resembles the magnetic susceptibility for CeRhSi_2 , a nonmagnetic IV system with similar Ce valence, in which Ce ions occupy only one lattice site.⁴³

Based on the Coqblin–Schrieffer model for orbitally degenerate Ce^{3+} ions, the Kondo temperature T_K describing the rate of spin fluctuations arising from hybridization of Ce $4f$ and conduction band states is related to the characteristic temperature T_0 as follows: $T_K = 2\pi T_0 W(N)/N$, where the degeneracy factor $N=6$ ($N=2j+1$) and the Wilson number $W(N=6)=0.6464$.^{55,56} Therefore, the performed analysis of the magnetic susceptibility of $\text{Ce}_2\text{Rh}_3\text{Sn}_5$ gives an estimate of the Kondo temperature for Ce2 ions of 189 K.

Finally, from the $\chi(T)$ data we conclude that the low temperature magnetic properties of $\text{Ce}_2\text{Rh}_3\text{Sn}_5$ can be explained as a superposition of the enhanced Pauli paramagnetism ($\chi(0) \approx 0.003$ emu/mol) due to delocalized $4f$ electrons of Ce2 ions and a magnetic order followed by local moment paramagnetic behaviour resulting from the presence of well localized magnetic moments of trivalent Ce1 ions. To further test this scenario, we performed specific heat measurements.

E. Specific heat

Fig. 6 shows the low temperature specific heat data for $\text{Ce}_2\text{Rh}_3\text{Sn}_5$. A distinct anomaly in the $C_p(T)$ curve at 2.4 K and a shoulder at 2.9 K are consistent with results of magnetic measurements (see Section III D) and indicate that $\text{Ce}_2\text{Rh}_3\text{Sn}_5$ undergoes two magnetic transitions. However, the low temperature specific heat is dominated by a broad contribution underneath the magnetic peaks. To inspect its origin, we perform quantitative analysis of different contributions to the low temperature specific heat.

First we evaluate the lattice and electronic specific heat. To this end, we plotted the C_p data in a $C_p(T)/T$ representation (see Fig. 6b) and applied the Debye model. At temperatures between ~ 11 K and ~ 20 K, the experimental data follows the dependence $C_p/T = \gamma + \beta T^2 + \delta T^4$, where the Sommerfeld coefficient $\gamma \approx 110$ mJ/(mol K²) accounts for the electronic part of the specific heat and the consecutive two terms with $\beta \approx 1.66 \times 10^{-3}$ mJ/(mol K⁴) and $\delta \approx 4.04 \times 10^{-7}$ mJ/(mol K⁶) represent the first two terms in the Taylor expansion for the lattice specific heat. Although the fit was performed on the specific heat data at rather high temperatures, we note that the upper limit of the temperature range used for this analysis is only of 25% of the temperature at which $\chi_{\text{Ce2}}(T)$ shows a maximum due to spin excitations from Kondo singlet ground state to $j=5/2$ multiplet for nonmagnetic Ce ions (see Section III D). Further, the obtained β value corresponds to the Debye temperature of 227 K, which is close to Debye temperatures reported by Patil *et al.*²⁸ for isostructural and isoelectronic compounds with other rare earth elements.

To check whether the estimated γ value correlates with the enhancement of the zero–temperature magnetic susceptibility $\chi(0) \approx 3 \times 10^{-3}$ emu/mol (see Section III D) and thus could be explained as due to itinerant f electrons in the FL state, we calculate the Sommerfeld–Wilson ratio $R_{\text{SW}} = \pi^2 k_B^2 \chi(0) / (3\mu_{\text{eff}}^2 \gamma)$ using the free-ion value of the effective fluctuating moment μ_{eff} of $2.54\mu_B$ per Ce^{3+} ion. The resulting $R_{\text{SW}} \approx 1$ is typical for HF systems in which strong hybridization between $4f$ and conduction band states leads to the delocalization of the $4f$ electrons, giving rise to an enhancement of the effective mass at low temperatures.⁵⁷

The magnetic specific heat $C_m(T)$ was calculated by subtracting from the total $C_p(T)$ the estimated lattice and electronic contributions (see Fig. 6a). The $C_m(T)/T$ was extrapolated to $T = 0$ and then integrated with respect to temperature to give an estimate for the low temperature magnetic entropy, $S_m(T)$. As shown in the inset of Fig. 6b, the $S_m(T)$ saturates at the value of $0.8 \text{ Rln}2$ per formula unit. Even with the electronic specific heat term γT included in the estimate, the magnetic entropy is only of $\text{Rln}2$ per formula unit containing two Ce ions. This result implies that only half of Ce ions in $\text{Ce}_2\text{Rh}_3\text{Sn}_5$ is in a CEF doublet ground state and contributes to the

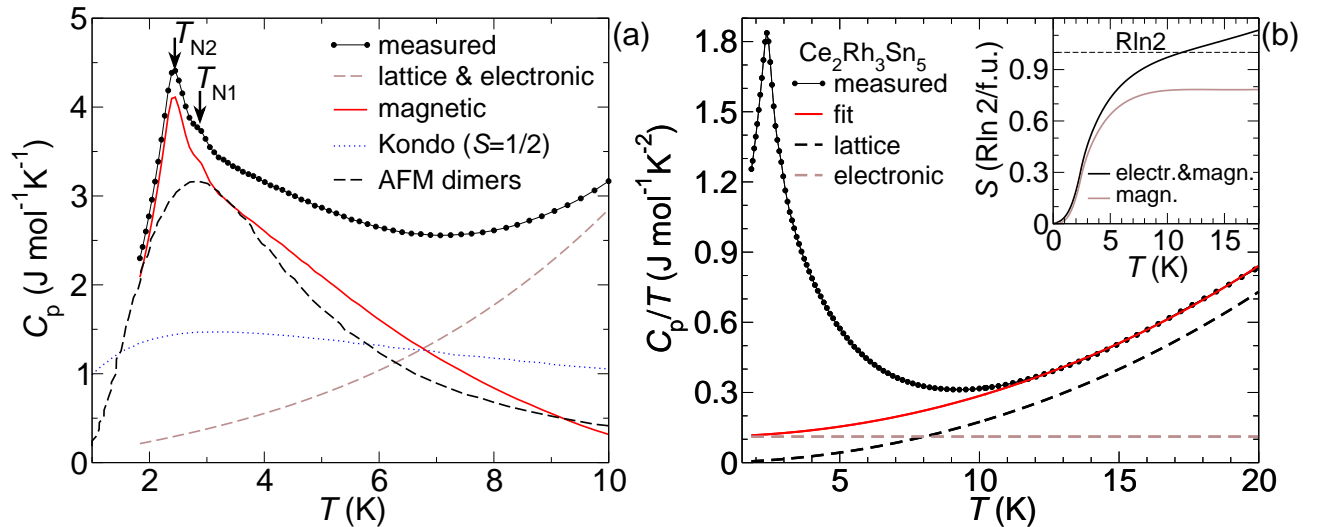


FIG. 6. (Color online) Low temperature specific heat of $\text{Ce}_2\text{Rh}_3\text{Sn}_5$ shown as $C_p(T)$ (panel a) and plotted in a conventional $C_p/T(T)$ representation (panel b). The experimental data (black circles) are shown together with results of fits based on Debye model as described in the text. The magnetic contribution (red solid line) as well as fits based on Kondo model for $S = 1/2$ ⁵⁹ (blue dots) and simulation of the magnetic specific heat of AFM dimers (black dashed line) are also presented in panel a. The inset in panel b depicts the entropy per formula unit of $\text{Ce}_2\text{Rh}_3\text{Sn}_5$ calculated from magnetic specific heat (solid brown line) and based on the sum of the electronic and magnetic specific heat (black solid line). The dashed horizontal line indicates the value of $R\ln 2$ expected for one Ce ion a magnetic doublet ground state.

low temperature magnetic ordering.

The magnetic entropy saturates well above the magnetic transitions only, at $T \approx 10$ K (see inset of Fig. 6b). Importantly, the value of the S_m recovered at $T_{N2}=2.9$ K is only of $0.40 R\ln 2$ per formula unit. Such a strong reduction of the magnetic entropy can be attributed to the Kondo effect on magnetic Ce ions and/or short range magnetic correlations that develop above magnetic ordering temperature. Assuming that the effect results solely from partial quenching of Ce $4f$ -derived magnetic moments of Ce^{3+} ions by Kondo effect, the single-ion Kondo temperature for magnetic Ce ions estimated based on model calculations of Yashima *et al.*⁵⁸ for $S = 1/2$ Kondo impurity should be of 7 K. However, attempts to describe the broad contribution to the magnetic specific heat based on the Kondo model⁵⁹ do not give satisfactory results (see Fig. 6a). Instead, the shape of the $C_m(T)$ resembles magnetic anomalies observed for low dimensional systems.^{60,61} As an example, Fig. 6a presents magnetic specific heat simulated for a system of AFM dimers with $S = 1/2$ assuming that exchange coupling inside the dimers $J/k_B \approx 5.7$ K and 75% of the magnetic Ce ions are involved in the short range order. Close similarity between the calculated curve and the magnetic specific heat hints at a dominance of an AFM coupling between local moments of nearest neighbouring Ce^{3+} ions. On the other hand, a layered crystal structure of $\text{Ce}_2\text{Rh}_3\text{Sn}_5$ composed of B blocks with trivalent Ce1 ions separated by A fragments containing nonmagnetic Ce2 ions (see Section III A) may facilitate quasi-two-dimensional magnetic correlations. Further studies including neutron diffraction and inelastic scattering

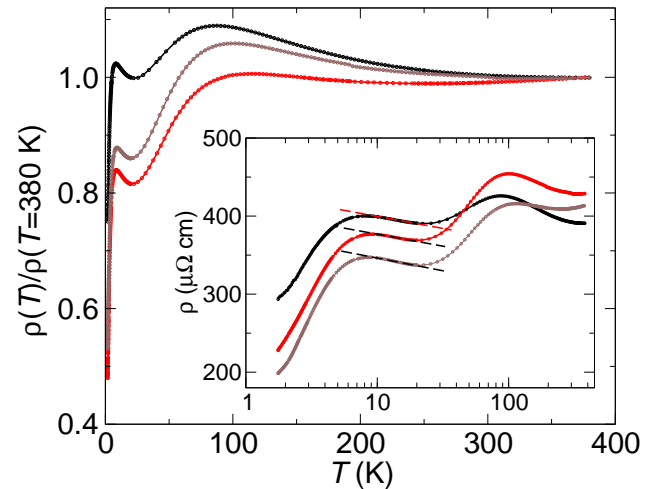


FIG. 7. (Color online) The electrical resistivity of $\text{Ce}_2\text{Rh}_3\text{Sn}_5$ measured on three different polycrystalline blocks normalized to the value of the resistivity at 380 K. The inset shows the $\rho(T)$ data plotted as a function of temperature on a logarithmic scale.

measurements are needed to inspect in detail the low temperature magnetic order and magnetic excitations in $\text{Ce}_2\text{Rh}_3\text{Sn}_5$.

F. Electrical resistivity

Fig. 7 shows the temperature dependence of the electrical resistivity measured on three polycrystalline blocks of $\text{Ce}_2\text{Rh}_3\text{Sn}_5$. The overall shape of the $\rho(T)$ curves in conjunction with the values of the resistivity of $\sim 200\text{--}300 \mu\Omega \text{ cm}$ at lowest temperatures indicate a metallic behaviour of $\text{Ce}_2\text{Rh}_3\text{Sn}_5$, as expected based on the thermodynamic and spectroscopic data, and in agreement with previous report.²⁸

For all the investigated specimens, the electrical resistivity shows broad maxima at $T \sim 100 \text{ K}$. At similar temperatures the XAS study revealed the fastest changes in Ce valence (see Section III B) and the $\chi_{\text{Ce2}}(T)$ shows maximum due to excitations from Kondo singlet ground state to $j=5/2$ multiplet (see Section III D). Therefore, we explain the strong scattering in this temperature range as due to both charge and spin fluctuations associated with intermediate-valent Ce ions. Similar pronounced contributions to $\rho(T)$ were observed for many Ce-based IV systems.^{6,43}

At lower temperatures, the $\rho(T)$ increases with decreasing temperature in a logarithmic fashion, as indicated in the inset of Fig. 7. Such logarithmic upturns signify the dominance of the $-\ln T$ term resulting from incoherent Kondo scattering of conduction electrons on magnetic Ce ions.

Finally, the $\rho(T)$ curves pass through maxima at temperatures of 8 K and fall rapidly with decreasing temperature. Such a temperature dependence of the resistivity is a typical manifestation of an onset of coherence between Kondo scattering centres arranged periodically in a crystal lattice.⁶² The development of coherence governs the $\rho(T)$ at temperatures close to the magnetic transitions, which may explain the lack of evidence for the magnetic transitions in the electrical resistivity curves.

G. Fixed spin moment calculations

To get insight into magnetic properties of $\text{Ce}_2\text{Rh}_3\text{Sn}_5$ from first principles, we performed a series of electronic band structure calculations within the LSDA approximation using the fixed spin moment (FSM) method.⁶³ This computational technique allows to fix the total magnetic spin moment of a system and adds this constraint to the DFT treatment.

Fig. 8 shows the total energies computed for different values of the FSM assuming the experimental crystal structure of $\text{Ce}_2\text{Rh}_3\text{Sn}_5$. The calculations indicate that the nonmagnetic state has the lowest total energy, but there is a flat region in the total energy-versus-FSM curve ranging from 0 to about $0.4 \mu_B/\text{f.u.}$, suggesting a proximity of a magnetic state.

Since calculated magnetic properties are often sensitive to atomic coordinates, we performed their computational relaxation based on atomic forces⁶⁴ to find theoretical equilibrium atomic positions for the LDA approximation.

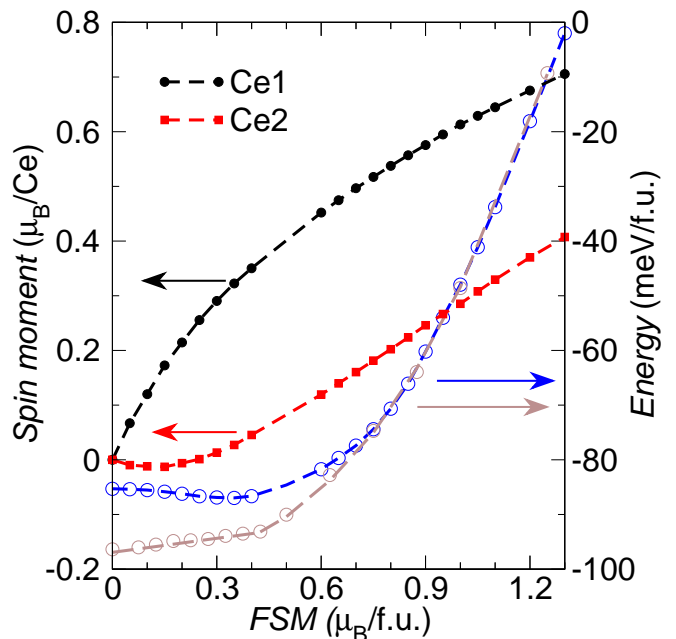


FIG. 8. (Color online) The total energy-versus-FSM curves derived from FSM calculations for $\text{Ce}_2\text{Rh}_3\text{Sn}_5$ within the LSDA approximation assuming either the experimental crystal structure (empty beige circles) or the LDA crystal lattice (filled blue circles). The FSM values represent the total magnetic spin moments per formula unit. The total energy scale was shifted to allow for direct comparison of the curves obtained for the experimental and LDA crystal structures. The calculated values of Ce1 and Ce2 spin moments are shown as black circles and red squares, respectively. For the experimental crystal structure the symbols are empty, whereas for the LDA crystal lattice they are filled. The dashed lines are guided to the eye. The thin vertical dashed-dotted line separates FSM solutions with negligible spin polarization on Ce2 sites (on the left side) from those with Ce2 spin moment of at least $0.1 \mu_B$ (on the right side).

The resulting internal coordinates for which total force on each atom is smaller than 5 mRy/a.u. are listed in Table II. For this relaxed crystal structure, the LSDA calculations with initial spin-polarization converged to a magnetic state, in agreement with the results of thermodynamic measurements (see Sections III D, III E). FSM calculations show that there is a shallow magnetic minimum in the energy-versus-FSM curve at the FSM value of $0.35 \mu_B/\text{f.u.}$, that has now slightly lower total energy than the nonmagnetic solution ($\Delta E \approx 1.7 \text{ meV/f.u.}$; see Fig. 8). Remarkably, the magnetic moment of $0.35 \mu_B/\text{f.u.}$ is carried basically only by Ce1 atoms, whereas Ce2 atoms as well as all Rh and Sn atoms in $\text{Ce}_2\text{Rh}_3\text{Sn}_5$ stay almost unpolarized (spin moments below $0.05 \mu_B$ per atom).

Obviously the detailed shape of the calculated energy-versus-FSM curve should depend not only on the atomic positional parameters but also on the lattice parameters. Furthermore, the symmetry lowering required by various possible spin arrangements may also affect slightly

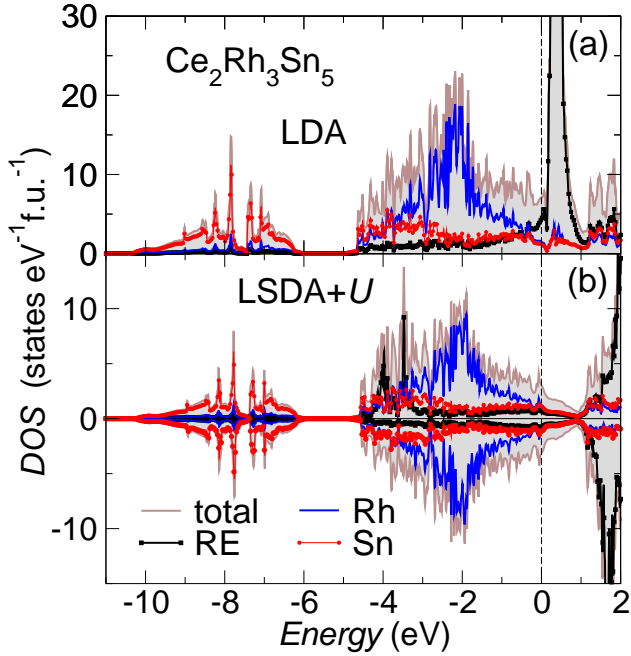


FIG. 9. (Color online) The total and atomic resolved DOSs for $\text{Ce}_2\text{Rh}_3\text{Sn}_5$ calculated within the LDA approximation (panel a) and using the LSDA+ U approach for the Ce 4 f shell (panels b,c) with $U_{\text{eff}} = 6$ eV⁶⁵ (panel b; thin lines with dots in panel c) or $U_{\text{eff}} = 3$ eV (thick solid lines in panel c).

the calculated total energy-versus-FSM curves. Nevertheless, the performed calculations for the experimental and the relaxed crystal structures indicate there is a notable energy cost associated with inducing spin polarization on Ce2 sites in $\text{Ce}_2\text{Rh}_3\text{Sn}_5$ (Fig. 8). The minimum difference in total energy between FSM calculations giving magnetic spin moment for Ce2 below $\sim 0.05 \mu_B$ (FSM $< 0.45 \mu_B/\text{f.u.}$; region on the left side of the vertical line on Fig. 8) and calculations resulting in spin polarization on Ce2 sites of at least $0.1 \mu_B$ per Ce2 (region on the right side of the vertical line on Fig. 8) is of 3.5 meV/f.u. Furthermore, for FSM calculations resulting in magnetic spin moment for Ce2 of $0.1 \mu_B$, the calculated moments on Ce1 sites are of $0.35\text{--}0.45 \mu_B$. Therefore, we conclude that Ce1 ions should bear magnetic moments and contribute to the low temperature magnetic ordering in $\text{Ce}_2\text{Rh}_3\text{Sn}_5$, whereas the Ce2 ions should remain nonmagnetic.

H. Valence band

Fig. 9 shows the total and partial atomic resolved DOSs for $\text{Ce}_2\text{Rh}_3\text{Sn}_5$ calculated for the experimental crystal structure within the LDA approximation and using the LSDA+ U approach to account for the strong Coulomb interaction within Ce 4 f shell. The valence band of $\text{Ce}_2\text{Rh}_3\text{Sn}_5$ consists of two parts separated by the gap of 1.5 eV. The structure at binding energies ranging

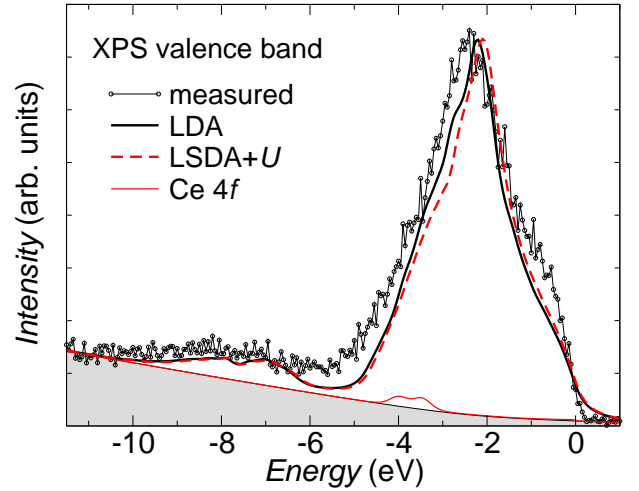


FIG. 10. (Color online) XPS valence band spectrum of $\text{Ce}_2\text{Rh}_3\text{Sn}_5$ (thin black solid line with dots) in comparison with theoretical spectra calculated based on partial DOSs obtained within the LDA approximation (thick black line) and using the LSDA+ U ($U_{\text{eff}} = 6$ eV)⁶⁵ approach for the Ce 4 f shell (thick dashed red line). The thin red (grey) solid line shows the sum of partial Ce1 4 f and Ce2 4 f contributions. The grey field represents background estimated using Tougaard algorithm⁵⁰.

from 5 to 8 eV originates primarily from 5 s states of Sn atoms. The main part of the valence DOS is dominated by hybridized Rh 4 d and Sn 5 p states.

Within the LDA approximation, the Ce 4 f states of both Ce1 and Ce2 form narrow bands with the centre of gravity above the Fermi level (see Fig. 9a). The calculated number of 4 f electrons for Ce1 ions equals 1.01. Thus, the electronic configuration of Ce1 is very close to 4 f^1 expected for Ce^{3+} . For Ce2 ions, however, the number of occupied 4 f states is of 0.92. Such a reduced occupation of the Ce2 4 f shell suggests a small deviation from the trivalent configuration, in line with a valence slightly larger than 3+ revealed by our XAS measurements (see Section III B).

Since the LDA method underestimates the Coulomb repulsion of electrons within narrow bands, we performed also additional band structure calculations using the LSDA+ U approach to account for stronger Coulomb interaction within Ce 4 f shell. Inclusion of the Hubbard-like interaction terms to the XC potential results in a shift of the occupied Ce 4 f bands toward higher binding energies and of the unoccupied 4 f states above the Fermi level for Ce ions in both lattice sites. As an example, Fig. 9c shows the partial DOSs for Ce1 and Ce2 calculated using the LSDA+ U method assuming $U_{\text{eff}}=3$ eV or $U_{\text{eff}}=6$ eV.

Our calculations show that for Ce1 the application of the U_{eff} parameter larger than ~ 2 eV yields the qualitatively correct physical picture of Ce^{3+} with magnetic spin moments of $1 \mu_B/\text{Ce}$ and the occupied 4 f states forming narrow bands well below the E_F . In case of Ce2, how-

ever, somewhat larger values of the U_{eff} of at least 3 eV were required to suppress the hybridization of the Ce2 4*f* and valence band states near the Fermi level and to move the 4*f* bands away from the Fermi energy. We note that for $U_{\text{eff}} \gtrsim 3$ eV the binding energies of the occupied 4*f* states are smaller by about 0.5 eV for Ce2 than for Ce1, independent of the exact value of the U_{eff} parameter (see Fig. 9c). Furthermore, the changes in the Ce2 4*f* bands induced by application of the LSDA+*U* approach lead to a narrowing of the main part of the valence band and result in a shift of 4*d* states of Rh2 and Rh3 towards lower binding energies, whereas the strength of correlation effects within the 4*f* shell of Ce1 ions has almost no impact on the other valence band states (not shown). Thus, the computational study gives an indirect evidence for the importance of the hybridization between Ce2 4*f* and conduction band states in Ce₂Rh₃Sn₅.

To shed light on the effective mass enhancement in Ce₂Rh₃Sn₅, we estimate bare values of the Sommerfeld coefficient $\gamma_b = (\pi^2/3)k_B \text{DOS}(E_F)$ using the $\text{DOS}(E_F)$ derived from our calculations of 6–7 st./(eV f.u.) (Fig. 9). The obtained γ_b values of 15–17 mJ/(mol K²) are about seven times smaller than the experimental Sommerfeld coefficient in the paramagnetic region of 110 mJ/(mol K²) (see Section III E). Different effects such as phonon–electron coupling or low-lying magnetic excitations can enlarge the bare γ_b value. However, such a strong enhancement of the Sommerfeld coefficient suggests that there is a notable renormalization of the effective quasiparticle masses due to dynamic electron–electron correlations. Since the applied computational methods (LDA and LSDA+*U*) are static mean–field approximations, by definition they neglect all dynamic correlation effects such as renormalization of electronic bands and the formation of Abrikosov–Suhl resonance. Therefore, we conclude that none of our calculations gives a proper description of the electronic structure of Ce₂Rh₃Sn₅ in a region close to the Fermi level. Further theoretical study based on dynamical mean–field theory (DMFT) is needed to inspect in detail the shape of the DOS in the vicinity of the Fermi energy for Ce₂Rh₃Sn₅.

In order to gain experimental insight into the valence band of Ce₂Rh₃Sn₅, we performed photoemission measurements. Fig. 10 shows the XPS valence band spectrum for Ce₂Rh₃Sn₅. To facilitate its comparison with the band structure results, the theoretical XPS spectra were estimated based on the calculated partial DOSs as described in Section II B. The commonly used Tougaard–type⁵⁰ background (grey field in Fig. 10) was added to the calculated data to account for the presence of secondary electrons during photoemission processes. The exemplary results obtained based on DOSs calculated within the LDA approximation and using the LSDA+*U* ($U_{\text{eff}} = 6$ eV) approach are presented in Fig. 10.

The calculated curves reflect all the essential features present in the measured XPS valence band spectrum, including the energy gap between the Sn 4*s*-like shallow core states and the remainder of the valence band. Thus,

the experiment confirms the reliability of our computational results. Although the LDA approximation seems to give a slightly better match regarding energy positions of the main features in the XPS valence band spectrum than the LSDA+*U* approach, the limited energy resolution of the performed XPS experiment prevents more detailed comparisons. Further, the Ce 4*f* contributions to the XPS valence band spectrum are very small as compared to the contributions from the other valence band states (Fig. 10). Therefore, the performed experiment also cannot give direct information about the localization of the Ce 4*f* states in the conduction band of Ce₂Rh₃Sn₅.

IV. CONCLUSIONS AND SUMMARY

The crystal structure of Ce₂Rh₃Sn₅ was refined from single crystal XRD data. Analysis of interatomic distances and coordination of Ce atoms occupying two distinct crystallographic sites suggests that Ce1 species are in a trivalent state (4*f*¹), whereas the valence of Ce2 ions should be larger than +3 due to extraordinarily short Ce2–Rh contacts. Electronic band structure calculations provide further indication for a trivalent state of Ce1 ions. By contrast, for Ce2 ions a reduced occupation of 4*f* states to ~ 0.92 suggests a small deviation from the trivalent electronic configuration. Importantly, XAS measurements revealed an IV behaviour. Assuming that Ce1 atoms are trivalent in the entire investigated temperature range, the valence of Ce2 species derived from the deconvolution of Ce *L*_{III} XAS spectra varies between +3.18 at 6 K and +3.08 at ~ 300 K.

Thermodynamic measurements revealed a magnetic ground state for Ce₂Rh₃Sn₅. Both specific heat and magnetization data show two magnetic transitions at $T_{N1} \approx 2.9$ K and $T_{N2} \approx 2.4$ K. The low temperature magnetic entropy of Rhn2 per formula unit implies, however, that only half of Ce ions in Ce₂Rh₃Sn₅ participates in the magnetic ordering. Electronic band structure calculations indicate that only Ce1 ions exhibit spin polarization in Ce₂Rh₃Sn₅. For Ce2 ions, the computational results in conjunction with the XPS spectra point to the importance of the hybridization of the 4*f* and conduction band states. This hybridization is crucial for the formation of a nonmagnetic Kondo–singlet state characterized by an enhanced Pauli–like magnetic susceptibility $\chi(0) \approx 0.003$ emu/mol and a large electronic specific heat $\gamma \approx 110$ mJ/(mol K²), which is about seven times larger than the bare γ_b value derived from the calculated single–particle $\text{DOS}(E_F)$. Such a strong augmentation of the Sommerfeld coefficient supports the important role of electron–electron correlation effects, whereas the Sommerfeld–Wilson ratio $R_{\text{SW}} \approx 1$ provides a further indication that both $\chi(0)$ and γ are similarly enhanced due to heavy quasiparticles in the FL state.

With increasing temperature, the strong Pauli–like behaviour in the magnetic susceptibility is going over to a local moment paramagnetism. Finally, near room

temperature $\text{Ce}_2\text{Rh}_3\text{Sn}_5$ behaves as an ordinary paramagnet with nearly full moment expected for all the Ce ions being in a trivalent state and a small positive $\chi_{0\text{-HT}} \approx 8 \times 10^{-5}$ emu/mol which, after correcting for core level diamagnetism and Landau diamagnetism, is comparable to the Pauli susceptibility expected based on the $\text{DOS}(E_F)$ derived from our electronic structure calculations.

To summarize, our combined experimental and theoretical study indicates that $\text{Ce}_2\text{Rh}_3\text{Sn}_5$ is a Kondo lattice system in which at low temperatures a magnetic order due to trivalent Ce1 ions coexists with an intermediate-valence behaviour of Ce2 ions with a non-magnetic Kondo-singlet ground state. Further study is needed to elucidate in detail the electronic band structure of $\text{Ce}_2\text{Rh}_3\text{Sn}_5$ near the Fermi level where dynamical

many-body effects determine the shape of quasiparticle DOS and to shed more light on the magnetic ground state.

V. ACKNOWLEDGMENTS

The authors thank Dr Christoph Geibel from Max-Planck Institute for Chemical Physics of Solids for fruitful discussions. The authors are grateful to Dr Jerzy Kubacki from University of Silesia for his kind help with XPS measurements and to Dr E. Welter and Dr D. Zajac from HASYLAB for their helpful assistance during XAS measurements on beamline C of Hasylab, Desy. M. G. would like to acknowledge financial support from the Max-Planck Society and the DAAD foundation through research fellowships.

-
- ¹ G. Stewart, *Rev. Mod. Phys.* **73**, 797 (2001); A. Georges, G. Kotliar, W. Krauth, and M. J. Rozenberg, *Rev. Mod. Phys.* **68**, 13 (1996), and references therein.
- ² A.C. Hewson in: *The Kondo Problem to Heavy Fermions*, Cambridge University Press (1997).
- ³ H.B. Radousky (Eds.) *Magnetism in Heavy Fermion Systems*, World Scientific Publishing Co. Ptd. Ltd., Singapore, 2000 (ISBN 981-02-4348-0).
- ⁴ P. Monthoux, D. Pines, and G.G. Lonzarich, *Nature* **450**, 1177 (2007).
- ⁵ G.R. Stewart, *Rev. Mod. Phys.* **78**, 743 (2006).
- ⁶ J.M. Lawrence, P.S. Riseboroughs, and R.D. Parks, *Reports on Progress in Physics* **44**, 1 (1981) and references therein.
- ⁷ M.A. Ruderman and C. Kittel *Phys. Rev.* **96**, 99 (1954).
- ⁸ S. Doniach in: R.D. Parks (Eds.) *Valence Instability and Related Narrow Band Phenomena*, Plenum New York (1977) and references therein.
- ⁹ T. Mishra, W. Hermes, U. Ch. Rodewald, R.-D. Hoffmann, R. Pöttgen, *Z. Anorg. Allg. Chem.* **634**, 470 (2008).
- ¹⁰ V. Eyert, E.-W. Scheidt, W. Scherer, W. Hermes, R. Pöttgen, *Phys. Rev. B* **78**, 214420 (2008).
- ¹¹ L. Durivault, F. Bourée, B. Chevalier, G. André, J. Etourneau, and O. Isnard, *J. Magn. Magn. Mat.* **232**, 139 (2001).
- ¹² F. Tappe, W. Hermes, M. Eul, R. Pöttgen, *Intermetallics* **17**, 1035 (2009).
- ¹³ S. Linsinger, M. Eul, W. Hermes, R.-D. Hoffmann, and R. Pöttgen, *Z. Naturforsch.* **64b**, 1345 (2009).
- ¹⁴ S.F. Matar, J.F. Riecken, B. Chevalier, R. Pöttgen, A. F. Al Alam, V. Eyert, *Phys. Rev. B* **76**, 174434 (2007).
- ¹⁵ J.A. Mydosh, A.M. Strydom, M. Baenitz, B. Chevalier, W. Hermes, R. Pöttgen, *Phys. Rev. B* **83**, 054411 (2011).
- ¹⁶ R. Feyerherm, E. Dudzik, K. Prokeš, J.A. Mydosh, Y.-K. Huang, and R. Pöttgen, *Phys. Rev. B* **90**, 041104 (2014).
- ¹⁷ J.M. Lawrence, M.F. Hundley, J.D. Thompson, G.H. Kwei, and Z. Fisk, *Phys. Rev. B* **43**, 11057 (1991).
- ¹⁸ O. Trovarelli, J.G. Sereni, G. Schmerber and J.P. Kappler, *Physica B* **206-207**, 243 (1995).
- ¹⁹ K. Ghosh, S. Ramakrishnan, S.K. Dhar, S.K. Malik, G. Chandra, V.K. Pecharsky, K.A. Gschneidner, Jr., Z. Hu, and W.B. Yelon, *Phys. Rev. B* **52**, 7267 (1995).
- ²⁰ M.B. Gamża, A. Ślebarski, and H. Rosner, *J. Phys.: Condens. Matter* **20**, 025201 (2008).
- ²¹ D. Niepmann, R. Pöttgen, B. Künnen, G. Kotzyba, C. Rosenhahn, and B.D. Mosel, *Chem. Mater.* **11**, 1597 (1999).
- ²² M.B. Gamża, A. Ślebarski, and H. Rosner, *Eur. Phys. J. B* **63**, 1 (2008).
- ²³ M.B. Gamża, W. Schnelle, R. Gumeniuk, Yu. Prots, A. Ślebarski, H. Rosner, Yu. Grin, *J. Phys.: Condens. Mat.* **21**, 325601 (2009).
- ²⁴ M.B. Gamża, W. Schnelle, A. Ślebarski, U. Burkhardt, R. Gumeniuk, and H. Rosner, *J. Phys.: Condens. Matter* **20**, 395208 (2008).
- ²⁵ M.B. Gamża *et al.*, to be published.
- ²⁶ A. Ślebarski, N.A. Frederick, and M.B. Maple, *Philos. Mag. B* **82**, 1275 (2002); A. Ślebarski, J. Spalek, M.B. Gamża, and A. Hackemer, *Phys. Rev. B* **73**, 205115 (2006); J. Spalek, A. Ślebarski, J. Goraus, L. Spalek, K. Tomala, A. Zarzycki, and A. Hackemer, *Phys. Rev. B* **72**, 155112 (2005).
- ²⁷ M.B. Gamża, A. Ślebarski, and H. Rosner *Eur. Phys. J. B* **67**, 483 (2009).
- ²⁸ N.G. Patil and S. Ramakrishnan, *Phys. Rev. B* **59**, 12054 (1999).
- ²⁹ M. Méot-Mayer, G. Venturini, B. Malaman, J. Steinmetz, and B. Roques, *Mat. Res. Bull.* **19**, 1181 (1984).
- ³⁰ See Supplemental Material at [URL] for details of powder X-ray diffraction measurements and metallographic investigations on polycrystalline samples of $\text{Ce}_2\text{Rh}_3\text{Sn}_5$.
- ³¹ R.C. Clark, and J.S. Reid, *Acta Cryst.* **A51**, 887 (1995).
- ³² P.J. Becker and P. Coppens, *Acta Cryst.* **A30**, 129 (1974).
- ³³ V. Petricek, M. Dusek and L. Palatinus, *Z. Kristallogr.* **229**, 345 (2014).
- ³⁴ B. Ravel and M. Newville, *J. Syn. Rad.* **12**, 537 (2005).
- ³⁵ Y. Baer, G. Bush and P. Cohn, *Rev. Sci. Instrum.* **46**, 466 (1975).
- ³⁶ K. Koepernik and H. Eschrig, *Phys. Rev. B* **59**, 1743 (1999).
- ³⁷ J.P. Perdew and Y. Wang, *Phys. Rev. B* **45**, 13244 (1992).

- ³⁸ H. Eschrig, K. Koepernik, and I. Chaplygin, *J. Solid State Chem.* **176**, 482 (2003).
- ³⁹ J.J. Yeh and J. Lindau, *At. Data Nucl. Data Tables* **32**, 1 (1985).
- ⁴⁰ R.V. Skolozdra, *Handbook on the Physics and Chemistry of Rare Earth* **24**, (167), 400, edited by Gschneider K A, Jr. and Eyring L, North-Holland, Amsterdam (1997).
- ⁴¹ J. Emsley, *The Elements*, Oxford Univ. Press (1998).
- ⁴² J.C. Fuggle, F.U. Hillebrecht, Z. Zolnierrek, R. Lässer, Ch. Freiburg, O. Gunnarsson and K. Schönhammer, *Phys. Rev. B* **27**, 7330 (1983); A.J. Signorelli and R.G. Hayes, *Phys. Rev. B* **8**, 81 (1973).
- ⁴³ D. Kaczorowski, A.P. Pikul, U. Burkhardt, M. Schmidt, A. Slebarski, A. Szajek, M. Werwiski, and Yu. Grin, *J. Phys.: Condens. Matter* **22**, 215601 (2010).
- ⁴⁴ R. Gumeniuk, R. Sarkar, C. Geibel, W. Schnelle, C. Paulmann, M. Baenitz, A.A. Tsirlin, V. Guritanu, J. Sichelschmidt, Yu. Grin, and A. Leithe-Jasper, *Phys. Rev. B* **86**, 235138 (2012); R. Sarkar, R. Gumeniuk, A. Leithe-Jasper, W. Schnelle, Yu. Grin, C. Geibel, and M. Baenitz, *Phys. Rev. B* **88**, 201101 (2013).
- ⁴⁵ I. Abbati, L. Braicovich, B. Michelis, A. Fasana, G.L. Olcese, F. Canepa, G.A. Costa, *Sol. St. Comm.* **55**, 1081 (1985).
- ⁴⁶ E.V. Sampathkumaran, *Hyperfine Interact.* **27**, 183 (1986).
- ⁴⁷ Chandan Mazumdar, R. Nagarajan, C. Godart, and R. Vijayaraghavan, *J. Appl. Phys.* **79**, 6347 (2016).
- ⁴⁸ U.B. Paramanik, Anupama, U. Burkhardt, R. Prasad, C. Geibel, and Z. Hossain, *J. Alloy. Comp.* **580**, 435 (2013).
- ⁴⁹ S. Doniach and M. Šunjić, *J. Phys. C* **3**, 285 (1970).
- ⁵⁰ S. Tougaard and P. Sigmund, *Phys. Rev. B* **25**, 4452 (1982).
- ⁵¹ O. Gunnarsson and K. Schönhammer, *Phys. Rev. B* **28**, 4315 (1983).
- ⁵² P.W. Selwood, *Magnetochemistry*, Interscience, New York (1956).
- ⁵³ S.M.M. Evans, T. Chung, and G.A. Gehring, *J. Phys.: Condens. Matter* **1**, 10473 (1989).
- ⁵⁴ V.T. Rajan, *Phys. Rev. Lett.* **51**, 308 (1983).
- ⁵⁵ N.E. Bickers, D.L. Cox, and J.W. Wilkins, *J. Magn. Magn. Mater.* **47-48**, 335 (1985) and references therein.
- ⁵⁶ A.C. Hewson and J.W. Rasul, *J. Phys. C: Solid State Phys.* **16**, 6799 (1983).
- ⁵⁷ P. Fulde, Routes to Heavy Fermions, in *Magnetism in Metals: A Symposium in Memory of Allan Mackintosh*, edited by D. F. McMorrow, J. Jensen, and H. M. Ronnow (Det Kongelige Danske Videnskabernes Selskab, Denmark, 1997), Vol. 45, p. 165.
- ⁵⁸ H. Yashima, H. Mori, N. Sato, and T. Satoh, *J. Magn. Magn. Mater.* **31-34**, 411 (1983).
- ⁵⁹ K.D. Schotte and U. Schotte *Physics Lett. A* **55**, 38 (1975).
- ⁶⁰ D.C. Mattis, *The Theory of Magnetism*, Harper & Row, New York, 1965.
- ⁶¹ A. Orendáčová, M. Kajňáková, J. Černák, J.-H. Park, E. Čizmar, M. Orendáč, A. Vlček, O.V. Kravchyna, A.G. Anders, A. Feher, and M.W. Meisel, *Chemical Physics* **309**, 115 (2005).
- ⁶² D.L. Cox and N. Greve, *Z. Phys. B - Condensed Matter* **71**, 321 (1988).
- ⁶³ K. Schwarz and P. Mohn, *J. Phys. F* **14**, L129 (1984).
- ⁶⁴ R. Yu, D. Singh, and H. Krakauer, *Phys. Rev. B* **43**, 6411 (1991).
- ⁶⁵ Y. Baer, H.R. Ott, J.C. Fuggle, and L.E. De Long, *Phys. Rev. B* **24**, 5384 (1981); J.K. Lang, Y. Baer, and P.A. Cox, *J. Phys. F* **11**, 121 (1981); J.F. Herbst, R.E. Watson, and J.W. Wilkins, *Phys. Rev. B* **17**, 3089 (1978); J.F. Herbst and J.W. Wilkins, *Phys. Rev. Lett.* **43**, 1760 (1979); V.I. Anisimov and O. Gunnarsson, *Phys. Rev. B* **43**, 7570 (1991) and references there in.

Coexistence of magnetic order and valence fluctuations in the Kondo lattice system $\text{Ce}_2\text{Rh}_3\text{Sn}_5$.

M. B. Gamża^{1,2,3}, R. Gumeniuk^{2,4}, U. Burkhardt², W. Schnelle², H. Rosner², A. Leithe-Jasper², and A. Ślebarski^{3,5}

¹*Jeremiah Horrocks Institute for Mathematics, Physics and Astrophysics,*

University of Central Lancashire, Preston PR1 2HE, UK

²*Max-Planck Institute for Chemical Physics of Solids, D-01187 Dresden, Germany*

³*Institute of Physics, University of Silesia, 40-007 Katowice, Poland*

⁴*Institute of Experimental Physics, TU Bergakademie Freiberg, 09596 Freiberg, Germany and*

⁵*Centre for Advanced Materials and Smart Structures, Polish Academy of Sciences, 50-950 Wrocław, Poland*

I. SUPPLEMENTARY INFORMATION

A. Metallographic study

The microstructures of the $\text{Ce}_2\text{Rh}_3\text{Sn}_5$ sample was inspected optically (Zeiss Axioplan 2) and with a scanning electron microscope (Philips XL 30). For the metallographic examination, a piece of about 3 mm diameter was cut from the annealed sample and embedded in conductive resin. Grinding was performed on abrasive papers (500- and 1000-grid silicon carbide). Polishing was done using slurries of 9, 3 and $1/4 \mu\text{m}$ diamond powder in alcohol-based lubricants.

Images of the sample surface obtained using the optical microscope with polarized light suggest that the sample consists of elongated grains with typical lengths of between $10 \mu\text{m}$ and $100 \mu\text{m}$ oriented randomly in various directions (see panels a and b of Fig. 1). Scanning electron microscopy investigations indicate that basically all the grains belong to the $\text{Ce}_2\text{Rh}_3\text{Sn}_5$ phase. Multiple images recorded from the same sample surface with a secondary electron detector and using a backscattered electron detector with magnifications ranging from $120\times$ to $4000\times$ did not detect impurity phases and shown only a uniform sample density.

The chemical composition was investigated by means of wavelength dispersive X-ray spectroscopy (WDXS) using a CAMECA SX100 electron microprobe equipped with a tungsten cathode. The local composition was determined by intensities of the X-ray lines $\text{Ce}L$, $\text{Sn}L$ and $\text{Rh}L$ which were excited by an electron beam of 20 nA at 15 keV. The X-rays were focused by large monochromator crystals PET (Pentaerythritol, $d = 0.437 \text{ nm}$) on a gas flow proportional counter. The proportions of the three elements were determined with respect to the appropriate reference materials Rh, Sn and CeAl_2 and resulted in analytical totals of 100.1(2) wt.% by using the PAP matrix correction model.¹ Measurements on ten points on the sample surface gave the same results within expected experimental error bars (see Table I). After averaging on the ten points, the following contents were obtained: Ce: 20.06(10) at.%, Rh: 29.95(19) at.%, Sn: 49.99(18) at.%. This composition corresponds to $\text{Ce}_{2.01(1)}\text{Rh}_{3.00(2)}\text{Sn}_{5.00(2)}$ and is in an excellent agreement with stoichiometric $\text{Ce}_2\text{Rh}_3\text{Sn}_5$.

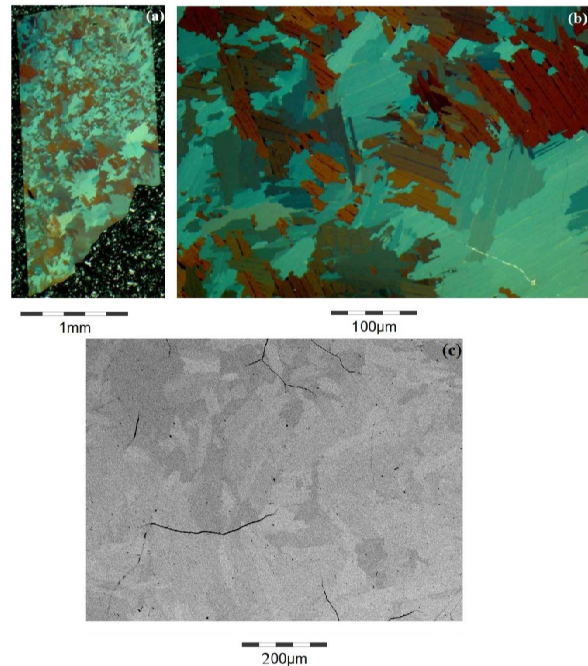


FIG. 1. Metallographic cross-section of an annealed ($800^\circ\text{C}/14 \text{ days}$) polycrystalline sample of $\text{Ce}_2\text{Rh}_3\text{Sn}_5$ showing orientation dependent reflectivity of the grains in optical (polarized light mode, panels a, b) and scanning electron (back scattered electron mode, panel c) micrographs.

B. X-ray powder diffraction

Phase analysis of the polycrystalline sample was carried out from X-ray powder diffraction patterns collected at room temperature on a HUBER imaging plate Guinier camera G670 using $\text{Cu } K\alpha_1$ radiation in a 2θ range of $3\text{--}115$ degrees with the expose time $6 \times 15 \text{ min}$. For powder XRD study, pieces of the sample were converted to a fine powder by grinding in a mortar with a small amount of acetone. Rietveld-type refinement of the powder pattern performed using Jana2006 program² gave atomic positional and displacement parameters consistent with results of our single crystal X-ray diffraction study. Lattice parameters derived from the refinement are: $a = 4.4992(1) \text{ \AA}$; $b = 26.4839(7) \text{ \AA}$;

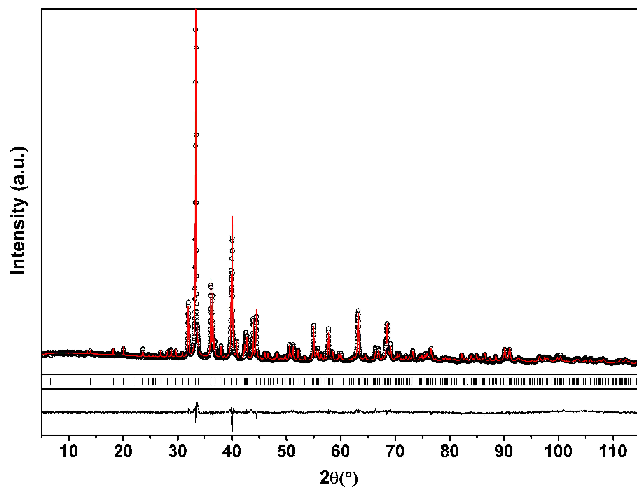


FIG. 2. X-ray powder diffraction pattern for $\text{Ce}_2\text{Rh}_3\text{Sn}_5$ (black circles) and Rietveld refinement (red lines) that resulted in the following statistical factors: $R(\text{all}) = 6.92$; $R_w(\text{all}) = 7.25$; $R_p = 5.17$; $R_{wp} = 6.59$.

TABLE I. Normalized atomic concentrations of Ce, Rh and Sn measured by WDXS method on ten points on the $\text{Ce}_2\text{Rh}_3\text{Sn}_5$ sample surface.

Nr.	Ce (at.%)	Rh (at.%)	Sn (at.%)
1	20.03	30.26	49.71
2	20.06	29.79	50.14
3	20.10	30.00	49.90
4	20.01	29.81	50.18
5	20.12	30.03	49.86
6	20.08	29.76	50.16
7	19.99	30.15	49.86
8	19.94	29.81	50.25
9	19.95	30.16	49.89
10	20.28	29.77	49.95

$c = 7.2160(2)$ Å. The sample was found to be nearly single phased. Apart from peaks originating from the $\text{Ce}_2\text{Rh}_3\text{Sn}_5$ phase, there are only few additional very slight features in the diffraction pattern, which we assign to a small amount of an unidentified minority phase (see Fig. 2).

¹ J.L. Pouchou and F. Pichoir, *Rech. Aerosp.* **3**, 13 (1984).

² V. Petricek, M. Dusek and L. Palatinus, *Z. Kristallogr.* **229(5)**, 345 (2014).